9
$B_{z,z}$ peak and trough analysis for rapid mapping of magnetisation direction

C.A. Foss and K.B. McKenzie

ABSTRACT

We present a simple, approximate method to estimate magnetisation direction from analysis of the vertical gradient of the vertical component of the magnetic field $B_{z,z}$ that can be derived from an FFT phase transform from TMI to B_z and an FFT gradient transform from B_z to $B_{z,z}$. The method can be applied semi-automatically (with supervision) to complete survey datasets to quickly detect distribution patterns of magnetisation from scattered anomalies. A key advantage is that the method is independent of the local geomagnetic field direction. We illustrate the method with synthetic data computed from ellipsoid models of different orientations, magnetisation directions and depths and then apply the method to survey data from a test area in eastern Queensland. The current limitations are principally due to challenges in isolation of the magnetic field variations from background fields and resolution limitations of regional aeromagnetic datasets.

9.1 INTRODUCTION

The direction of natural remanent magnetisation (NRM) of a rock is determined by ages, post-acquisition rotations and relative strengths of all its remanent magnetisation components. The resultant or 'total' magnetisation is the vector sum of NRM and an induced magnetisation approximately equal to the product of magnetic susceptibility and magnetic field strength and directed parallel to the local geomagnetic field. Direct determination of remanent and induced magnetisation strengths and directions is based on measurement of oriented rock samples but the resultant magnetisation strength and direction can also be estimated by analysis of magnetic field data. Some recent methodologies used to estimate direction of magnetisation over a compact source include the use of magnetic moments (Helbig 1963; Schmidt and Clark 1998; Phillips *et al*. 2007; Caratori Tontini and Pedersen 2008; Foss and McKenzie 2011; Clark 2012, 2013a, 2014); by inversion of magnetic moments (Medeiros and Silva 1995); from parametric inversion (Foss and McKenzie 2011; Pratt *et al.* 2014) or directly from the magnetic gradient tensor and its eigenvectors (McKenzie 2020).

The most reliable method of estimating magnetisation direction from magnetic field data is by focussed inversion of individual anomalies. However, inversions are time consuming. We would like to find more rapid methods to scan a complete magnetic survey dataset, even if the results are less reliable. In this chapter we propose such a method based on analysis of $B_{z,z}$ the vertical gradient of the vertical component of the field.

The total gradient (TG) and normalised source strength (NSS) transforms of measured TMI highlight sharp magnetic field variations due to shallow magnetisations and show only weak influence of source magnetisation direction. Outputs from the transforms are

simpler and more radially symmetric than the input TMI field and they peak over or close to horizontal centres of compact magnetisations (Beiki *et al*. 2012; Clark 2012, 2014; Foss and Austin 2023). Curvature analysis of surfaces (Blakely and Simpson 1986; Phillips *et al.* 2007) applied to gridded magnetic field data locates elongate ridges and troughs as well as equidimensional peaks and wells of those functions. For either TG or NSS transforms we only need to map positive curvature features, and for analysis of compact magnetisations we select equidimensional peaks. Estimation of magnetisation direction for sheet-like magnetisations that produce elongated ridges in the transform outputs is more complex and must be treated separately. Success of the TG and NSS transforms in locating magnetisations is in large part due to their restricted sensitivity to magnetisation direction. To subsequently estimate magnetisation direction from those located magnetisations we need either to return to the TMI data or to select an alternative transform that benefits recovery of magnetisation direction rather than suppresses it.

In an early study of three-dimensional TMI modelling of compact magnetic bodies, Zietz and Andreasen (1967) noted that in high inclination northern hemisphere geomagnetic fields the declination of magnetisation is indicated by the azimuth of the TMI peak-to-trough vector and the inclination of magnetisation is indicated by the amplitude ratio of the TMI peak and trough. In the northern hemisphere a TMI peak to trough ratio much greater than 1 indicates a steep positive inclination of magnetisation, a ratio close to 1 indicates a low-inclination magnetisation and a ratio much less than 1 indicates a steep negative inclination. In the southern hemisphere the roles of the TMI peak and trough are reversed because the sign of the field vector relative to the ground surface is reversed (the convention is that positive down describes the northern hemisphere field and the upward directed southern hemisphere field is negative). TMI is mostly perceived as a consistent magnetic field parameter but its orientation varies between survey locations with different geomagnetic inclination. Resultant magnetisation directions typically vary with geomagnetic inclination because of variation in the direction of their induced magnetisation components. However, even identical magnetisations produce different TMI anomalies in fields of different geomagnetic inclination because of differences in the vector addition with the local background field. The direction of the anomalous field varies substantially around and above a magnetisation and this dictates the anomaly pattern. To reduce this complication we use the field component B_z of fixed (vertical) orientation. Vertical orientation provides advantage because most magnetic fields are measured in a horizontal plane perpendicular to that direction. This is a similar advantage to that derived from use of the reduced to pole (RTP) FFT of TMI data. However, the standard RTP transform also attempts to rotate the magnetisation direction to vertical on assumption that it is initially parallel to the geomagnetic field (Baranov and Naudy 1964; Blakely 1995). The phase change on FFT from TMI to B_z or $B_{z,z}$ is independent of magnetisation direction. In unusual cases that the anomalous field is so strong that it significantly rotates the TMI direction across the region of the magnetic anomaly an intermediate step is required to iteratively adjust the field to a consistent direction as devised by Lourenço and Morrison (1973) and further developed by Schmidt and Clark (2006) and Clark (2013b). Use of the B_z component extends the relationships noted by Zietz and Andreasen (1967) in steep inclination fields. Figure 9.1 shows TMI anomalies (in the upper half of the figure) and B_z anomalies (in the lower half of the figure) due to a dipole with a magnetisation of declination 45° and inclination −45°. The patterns of the TMI anomalies of Figs 9.1A and 9.1C in steep downward (north pole) and steep upward (south pole) fields respectively are as predicted by the relationships of Zietz and Andreasen (1967). The TMI anomaly in the low-inclination equatorial field shown in Fig. 9.1B is quite different. All three B_z anomalies (Figs 9.1D, 9.1E and 9.1F) are identical, resulting from the scalar summation of anomalous and background B_z field components. The interpretational advantages of a single anomaly pattern for one magnetisation direction in all geomagnetic fields is considerable. Derivation of B_z from transformation of TMI data is not especially problematic, even in low geomagnetic inclination fields, provided the data quality and sample spacing are adequate. If these conditions are not met then analysis of the data by any method will be uncertain.

Definition of a B_z anomaly by separation from a background field is of similar difficulty and concern as for TMI data. A common and effective solution for both field isolations (although with escalation of other challenges) is through use of the vertical gradient. For the B_z field component this gradient is $B_{z,z}$. The background field is commonly assumed to contribute only longer wavelength variations and these produce significantly weaker gradients than shorter wavelength field variations of shallow anomalous magnetisations of interest. Conversely,

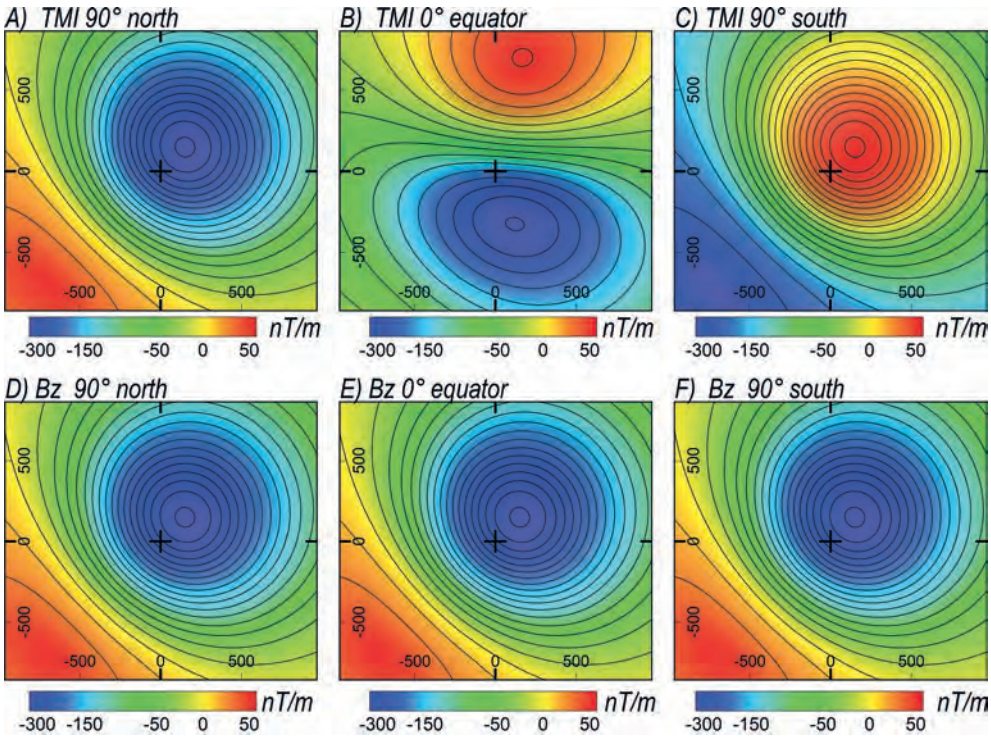

Fig. 9.1. Anomalies in different background fields over an 800 m radius sphere of magnetisation 1 A/m, declination D_M = 45°, and inclination I_M = −45° at a depth of 800 m. The top row are TMI anomalies, the bottom row are Bz anomalies.

investigation of the vertical gradient is problematic where there are significant superimposed shorter wavelength field variations or measurement imperfections. In these cases it can be of advantage to pre-condition the data with a mild upward continuation before estimating the vertical gradient. Use of the gradient can still be of advantage despite the contrary operations of upward continuation (a smoothing operator) and application of the gradient (a sharpening operator). Upward continuation is also more versatile and easily comprehended than the alternative use of fractional derivatives (Cooper and Cowan 2003). The sign of the vertical gradient with respect to the ground surface does not change with geomagnetic hemisphere and so the sign difference of B_z in southern and northern hemispheres persists in $B_{z,z}$ data.

9.2 THE VERTICAL GRADIENT OF THE VERTICAL FIELD COMPONENT: $B_{Z,Z}$

Figure 9.2 shows six $B_{z,z}$ anomalies for dipoles of different magnetisation direction. As already established, the pattern of these anomalies is independent of the direction of the field in which they are measured. The anomaly for a vertical upward magnetisation (Fig. 9.2A) has a trough to peak amplitude ratio of almost 20:1. The equivalent $B_{z,z}$ anomaly of a vertical downward magnetisation (Fig. 9.2B) is identical other than for a change of polarity. Unlike TMI anomalies, the prominent polarity of $B_{z,z}$ and B_z anomalies reveal if the magnetisation is upward directed (negative polarity) or downward directed (positive polarity) regardless of geomagnetic hemisphere. Anomalies of compact, horizontal, north–south magnetisations are symmetric with equal amplitude peak and trough. For a southerly directed (declination = 180°) horizontal magnetisation the anomaly has a peak to the north and trough to the south (Fig. 9.2E) and for northerly directed (declination = 0°) horizontal magnetisation the anomaly pattern is reversed with the trough to the north and peak to the south (Fig. 9.2F). For north or south directed intermediate inclinations the anomalies have a form intermediate between the anomalies due to vertical and horizontal magnetisations. These patterns are shown in Figs 9.1C and 9.1D for a pair of mid-range northerly directed magnetisations with inclination I_M = −45° and +45° respectively. The anomaly patterns of corresponding southerly directed magnetisations are rotated about a vertical axis by 180°.

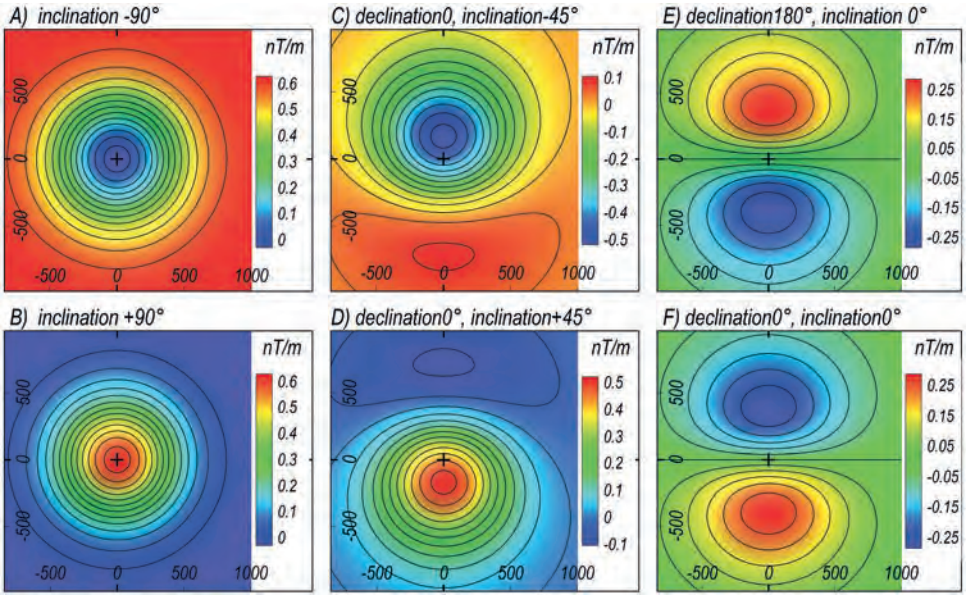

Fig. 9.2. Dipole $B_{z,z}$ anomalies of different magnetisation direction.

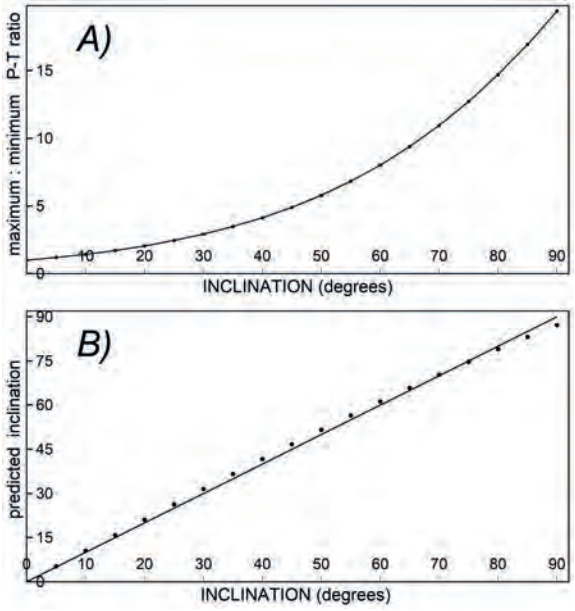

Fig. 9.3. A) peak to trough ratio against inclination of magnetisation, B) the same data (points) on a logarithmic scale with a linear predictor.

As illustrated in Figs 9.1 and 9.2, the declination of magnetisation is recorded by the peak to trough orientation of the B_z or $B_{z,z}$ anomalies. The dipole $B_{z,z}$ ratio of the prominent to weaker feature (the peak to trough ratio for a positive-inclination magnetisation or the trough to peak ratio for a negative-inclination magnetisation) is plotted against inclination in Fig. 9.3A. The ratio increases smoothly from 1 for a horizontal inclination to almost 20 for a vertical inclination. Figure 9.3B shows the same data plotted as points on a logarithmic amplitude scale, together with a straight-line approximation. This linear prediction of inclination (value = 0 at 0° inclination and 1.34 at 90° inclination) with an average departure from the true inclination of only 0.5° and a maximum departure of less than 2° is adequate for approximate estimation of the inclination of magnetisation.

For a dipole source, the $B_{z,z}$ peak and trough also provide an estimate of depth to the dipole (the centre of a spherical source). The distance between peak and trough varies with inclination of magnetisation. The peak and trough are closest for a zero-inclination magnetisation with a separation of 78% of the depth to centre of magnetisation. For steep inclinations the separation increases to 115%. The conversion factor to estimate centre depth from peak and trough separation is plotted in Fig. 9.4. The centre point of a dipole magnetisation lies on a line joining the $B_{z,z}$ peak and trough of the anomaly with a relative distance from each that is approximately inversely proportional to their amplitudes. For a zero-inclination magnetisation the horizontal centre of magnetisation is midway between the equal amplitude peak and trough. The departure from this approximation is plotted in Fig. 9.5. For an inclination of magnetisation of ± 35° the predicted centre of magnetisation is just over 1% of the peak to trough separation closer to the higher

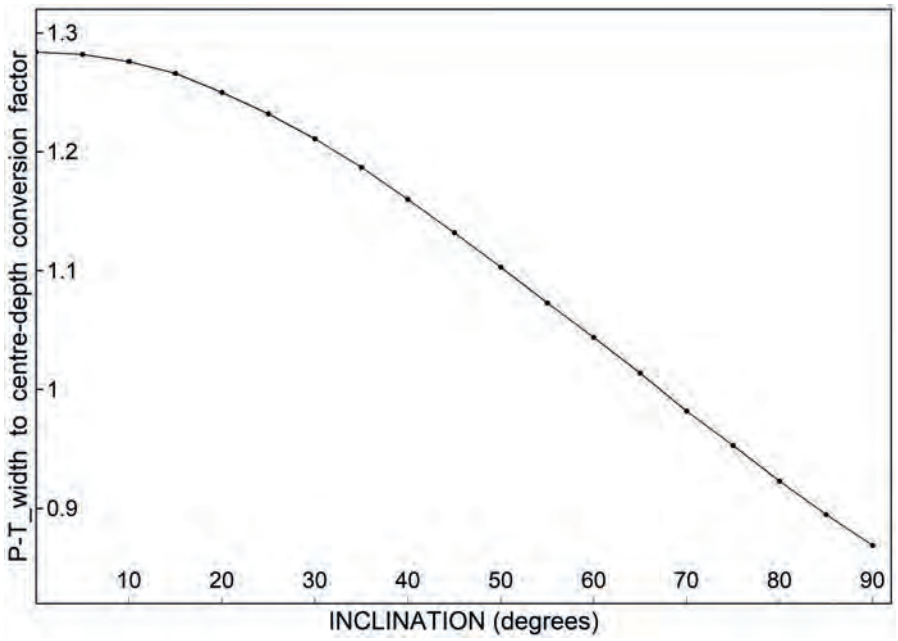

Fig. 9.4. Conversion factor to estimate depth to a dipole centre from the Bz,z peak and trough separation as a function of the inclination of magnetisation.

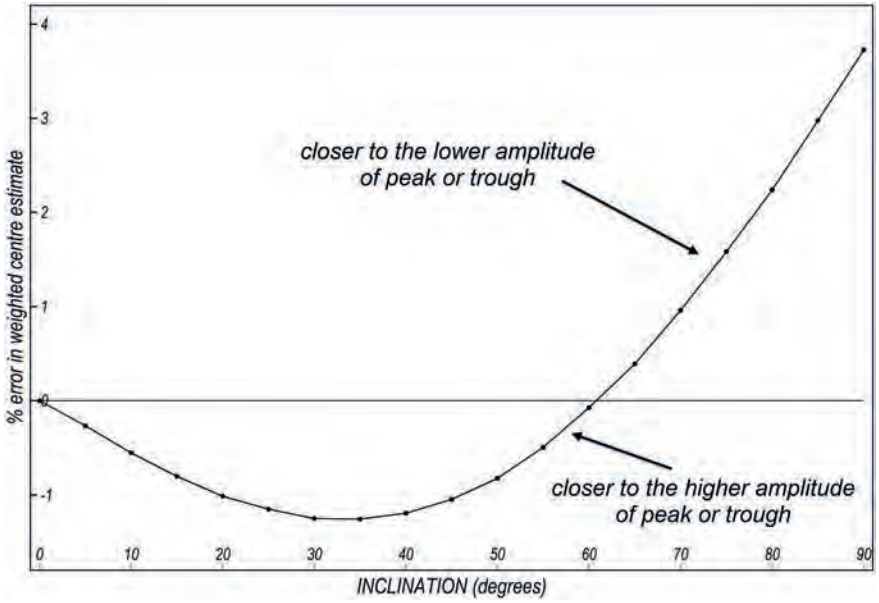

Fig. 9.5. Percentage error in weighted centre prediction of the horizontal centre of magnetisation.

amplitude feature. For an inclination of 61° the prediction is correct and at 90° the prediction is almost 4% closer to the lower amplitude feature than the true centre (for particularly steep magnetisations the distant, weak lower-amplitude feature is difficult to reliably locate and its exact inclination is imprecisely estimated).

9.3 A SYNTHETIC TEST STUDY USING ELLIPSOID SOURCES

A major concern for the magnetisation directions estimated by the proposed $B_{z,z}$ analysis is the validity in representing the distribution of magnetisation with a dipole model. Figure 9.6 illustrates a set of six prolate ellipsoids with axis radial lengths of 800 and 300 m (a

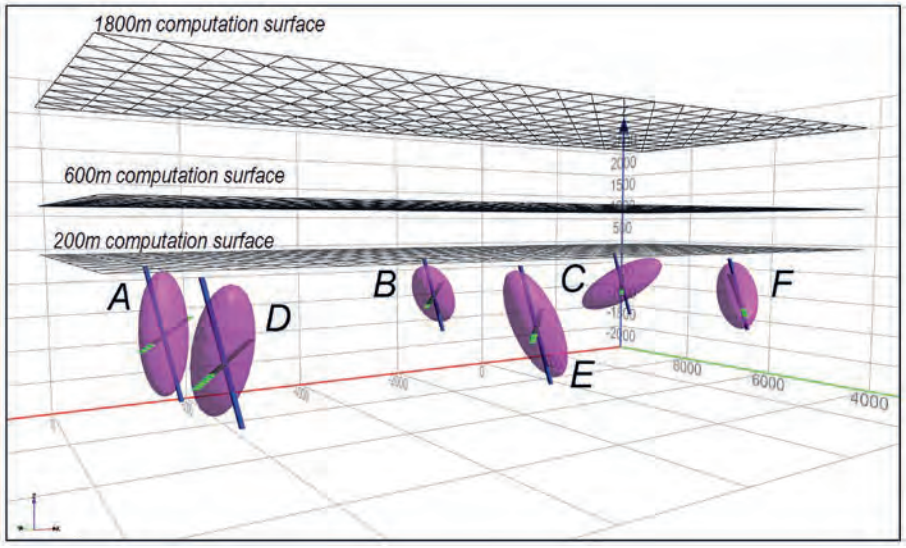

Fig. 9.6. Plunging ellipsoid magnetisation models (magenta) with upward directed magnetisation vectors (blue – steep inclination, green – low inclination). The spatial properties are listed in Table 9.1.

Table 9.1. Ellipsoid body properties list. X_0, Y_0, Z_0 are centre coordinates, the azimuth and dip describe the major axis.

BODY	X_0	Y_0	Z_0	Azimuth°	Dip°
A	–7000.0	7000.0	800.0	0	90
B	–3000.0	7000.0	709.0	0	60
C	1000.0	7000.0	478.0	45	30
D	–7000.0	4500.0	709.0	90	60
E	–3000.0	4500.0	478.0	315	30
F	1000.0	4500.0	478.0	225	30

2.7:1 ratio) and different plunge and azimuth. Expressions for the gradient tensor elements (including $B_{z,z}$) of a uniformly magnetised triaxial ellipsoid are given in McKenzie (2020) and for a right circular cylinder by McKenzie (2022). The prolate ellipsoids we use in this study are a special case of triaxial ellipsoids with two identical length minor axes and one major axis. We selected the six ellipsoids to investigate relationships between their plunge and azimuth angles with two magnetisation directions: A) a high-inclination magnetisation of –75° with a declination of 315° and B) a low-inclination magnetisation of –15° and declination of 45°. $B_{z,z}$ analysis is independent of declination of magnetisation angles relative to the magnetic field but the angle between direction of magnetisation and any spatial extension of the magnetisation has a significant influence on the anomaly shape. We adjusted the body centre depths to give a consistent depth to the tops of magnetisation of 200, 600 and 1,800 m respectively below three elevation surfaces at which we computed $B_{z,z}$. The purpose of computation at different elevations is to investigate attenuation of the influence of shape with increasing distance from the sources. In proximal fields shape influence is considerable but in distal fields the anomalies more closely approximate to those of dipoles of the same total magnetisation (see also Chapter 4).

Figure 9.7 shows images of $B_{z,z}$ for each of the six ellipsoids in Table 9.1 computed at the shallowest elevation of 200 m above the tops of the magnetisations for the steep inclination (I_M = -75°) magnetisation in Fig. 9.7A and for the low-inclination magnetisation (I_M = –15°) in Fig. 9.7B. Even at this proximity to the top of magnetisation (200 m compared to the long-axis length of the magnetisation of 1,600 m) the direction of magnetisation is the dominant influence on anomaly orientation as measured by the peak to trough azimuth (shown by the white arrows in Fig. 9.7). Peak to trough amplitude ratio is best estimated from contour overlays over the map images. The high trough to peak ratio of all the anomalies in Fig. 9.7A reveals the steep negative inclination of the source magnetisations for those anomalies and the near-unity peak to trough ratios of Fig. 9.7B reveal the low inclination of those source magnetisations. However, the peak to trough amplitude ratio is also influenced by body orientation relative to magnetisation direction. To perform the $B_{z,z}$ dipole analysis

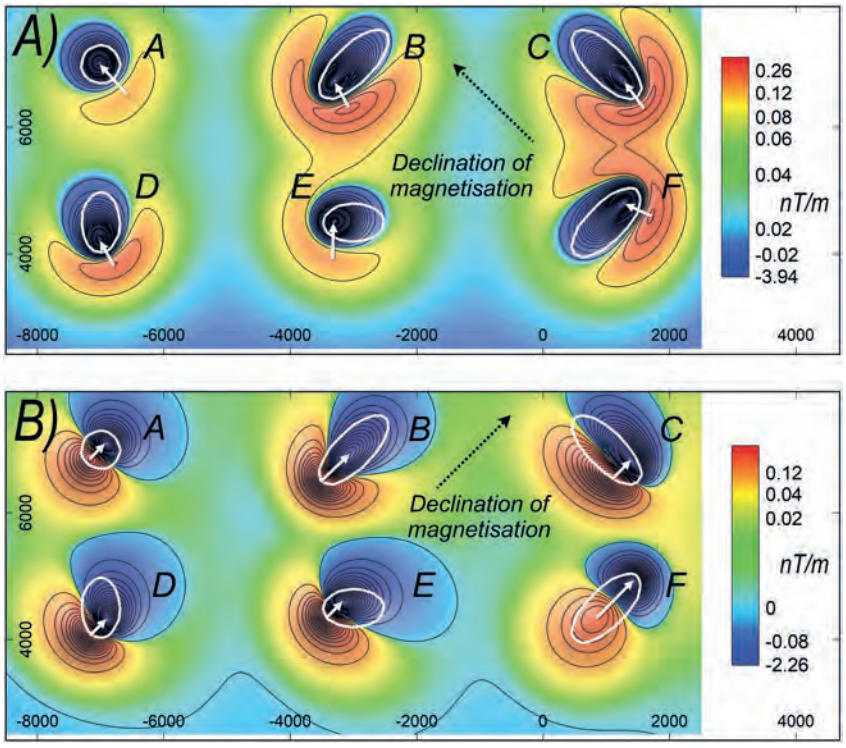

Fig. 9.7. $B_{z,z}$ anomalies for the ellipsoids in Fig. 9.6 with magnetisations of: A) inclination −75°, declination 315°, and B) inclination −15°, declination 45° computed at an elevation 200 m above the tops of the magnetisations. The white arrows are from anomaly maxima to minima.

Table 9.2. $B_{z,z}$ dipole analysis for anomalies of magnetisation: declination 315°, inclination −75°.

Elevation	Body	PT ratio	PT azimuth°	PT inclination°	error°	Centre offset	Centre azimuth°
1,800	A	13.77	314.6	−77.1	2.1	50.5	133.9
1,800	B	12.70	317.7	−74.7	0.8	161.9	168.2
1,800	C	12.07	321.3	−73.2	2.5	157.7	203.1
1,800	D	12.07	321.7	−73.2	2.6	158.6	203.2
1,800	E	11.89	315.4	−72.8	2.2	181.7	135.4
1,800	F	12.07	308.7	−73.2	2.5	155.5	67.1
600	A	17.50	315.0	−84.1	9.1	14.6	135.2
600	B	12.69	322.9	−74.7	2.1	232.5	177.6
600	C	10.16	330.2	−68.1	8.3	292.4	218.7
600	D	18.23	347.4	−85.3	11.3	234.3	263.6
600	E	9.94	315.0	−67.5	7.5	298.4	135.0
600	F	10.16	299.8	−68.1	8.3	292.4	51.3
200	A	27.48	314.9	−97.4	22.4	0.6	109.3
200	B	12.82	328.1	−75.0	3.4	299.4	179.6
200	C	8.21	333.4	−61.9	14.6	432.1	222.2
200	D	23.98	381.0	−93.4	16.7	312.4	268.9
200	E	7.85	315.1	−60.6	14.4	437.4	135.0
200	F	8.21	296.6	−61.9	14.6	432.1	47.8

Table 9.3. $B_{z,z}$ dipole analysis for anomalies of magnetisation: declination 45°, inclination −15°.

Elevation	Body	PT ratio	PT azimuth°	PT inclination°	error°	Centre offset	Centre azimuth°
1,800	A	1.74	45.0	−16.3	1.3	33.6	44.5
1,800	B	1.65	44.9	−14.7	0.3	91.8	168.7
1,800	C	1.60	45.0	−13.8	1.2	95.9	224.8
1,800	D	1.65	45.2	−14.7	0.4	92.4	280.9
1,800	E	1.70	45.0	−15.5	0.5	125.6	122.3
1,800	F	1.88	44.9	−18.5	3.5	166.4	45.0
600	A	1.81	45.0	−17.4	2.4	16.7	44.8
600	B	1.50	44.5	−11.9	3.1	200.6	179.4
600	C	1.27	45.0	−7.1	7.9	257.9	225.0
600	D	1.50	45.4	−11.9	3.1	200.8	270.7
600	E	1.63	44.9	−14.3	0.7	260.7	133.5
600	F	2.60	45.0	−28.1	13.1	304.6	45.0
200	A	1.91	45.0	−19.1	4.1	9.5	44.4
200	B	1.31	44.4	−8.0	7.1	286.6	180.8
200	C	0.90	45.0	3.1	18.1	425.2	225.0
200	D	1.31	45.5	−8.0	7.0	287.1	269.2
200	E	1.55	45.0	−12.8	2.2	408.4	135.0
200	F	4.87	44.9	−46.5	31.5	455.7	45.0

Table 9.4. Mean errors in magnetisation direction and centre point estimation of the $B_{z,z}$ analysis and dipole inversions at the three computation elevations.

		$B_{z,z}$ ANALYSIS RESULTS			INVERSION RESULTS		
Inclination of magnetisation	Elevation	Inclination error	Angular error	Centre offset	Inclination error	Angular error	Centre offset
High (A)	200	14	14	319	15	20	280
High (A)	600	7	8	227	7	11	198
High (A)	1,800	2.1	2.1	144	2.1	3.30	106
Low (B)	200	12	12	312	9.0	9.2	257
Low (B)	600	5	5	207	3.0	3.10	157
Low (B)	1,800	3.5	3.6	101	0.7	0.7	74

we computed $B_{z,z}$ grids for the bodies in Table 9.1 with both the steep-inclination and low-inclination magnetisations detailed above. We then applied algorithms based on Blakely and Simpson (1986) and Phillips *et al.* (2007) to locate the peaks and troughs of these grids and from those results determined distance and azimuth between adjacent peak and trough pairs and their amplitude ratio. We submitted these statistics to the $B_{z,z}$ dipole analysis to obtain the magnetisation direction estimates listed in Table 9.2 for the steep-inclination magnetisation and in Table 9.3 for the low-inclination magnetisation (in each case 18 estimates for the six bodies at the three elevations). Table 9.4 summarises the mean magnetisation errors and centre offsets from the analyses at each elevation. There is no significant difference in the performance of the analysis in recovering magnetisation direction or centre location from anomalies of the high- or low-inclination magnetisations (there may be sensitivities to directions outside the range we investigated of 15° to 75°). Consistent with reduction of shape effect with elevation, there is significant improvement of the $B_{z,z}$ magnetisation direction estimates with

increasing distance from the magnetisation. In practice it is challenging to fully realise this advantage because of the reduction of amplitude with increased distance from the magnetisation (particularly as we are using field gradients). If upward continuation is used to reduce source shape effects it is best to calculate the field gradients beforehand because at higher elevation the ratio of source gradients relative to the background field gradients is reduced.

The $B_{z,z}$ analysis presented above is based on simple dipole models of the distribution of magnetisation. From Table 9.4 we can see that for the 2.7:1 radial ratio ellipsoid models used, the errors in estimated magnetisation direction are less than 10° except at low elevations close to the magnetisations. We consider this acceptable, particularly as geological complexities and measurement imperfections limit the significance of analyses. To better understand the nature and limitations of the dipole basis of our analysis we also inverted the anomalies using dipole models. Figure 9.8A is a composite illustration of the six different ellipsoid models co-centred and with superimposed spherical (dipole) models from individual inversions of the model fields of those ellipsoids. The blue spheres are from inversion of B_z and the red spheres are from inversion of $B_{z,z}$. All bodies are given identical intensity of magnetisation (inversion of dipole sources is completely insensitive to independent values of volume and intensity of magnetisation and there is only low sensitivity for the ellipsoid models). The spherical B_z inversion models have centres of magnetisation that are shallower than the magnetisation centres of the input ellipsoid models and horizontally displaced in the up-dip direction. Because they are shallower, they also have a reduced magnetic moment to best-fit the deeper-centred ellipsoids. The $B_{z,z}$ inversions have a higher weighting to the shallowest magnetisation and migrate further from the centres of the input models. As a result they have even shallower and more horizontally displaced centre locations with further reduction of magnetic moments. It seems that the $B_{z,z}$ inversion models are less acceptable representations of the input magnetisations than the B_z inversion models. However, in application to measured field data the advantages of improved anomaly separation provided by use of gradients generally outweigh this disadvantage. This is particularly relevant in design of automated or semi-automated analysis to be applied to multiple anomalies across large distances with different background fields.

Figure 9.8B shows (in mesh view) an ellipsoid model from which an input field is computed and a co-centred spherical model of identical volume and magnetic moment. The red spherical model is derived from a $B_{z,z}$ inversion at an elevation of 200 m above the top of the magnetisation, the green model is from a $B_{z,z}$ inversion at 600 m above the top of the magnetisation and the blue model is from a $B_{z,z}$ inversion at 1,800 m above the top of magnetisation. The (red) smallest and most horizontally and vertically displaced spherical model from the shallowest field inversion has the highest error in estimated magnetisation direction. The higher and more distal models have progressively smaller offsets from the centre of the

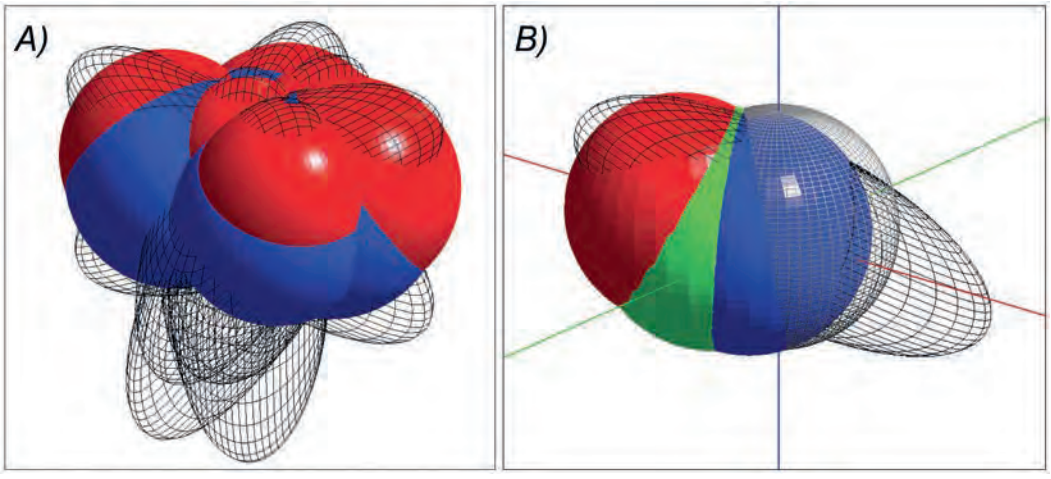

Fig. 9.8. A) co-centred plunging ellipsoid source models with dipole inversion models from individual inversion of the fields of those bodies: B_z inversions (in blue)and Bz,z inversions (in red) and B) Mesh models of a plunging ellipsoid and co-centred, equal volume sphere, with $B_{z,z}$ inversion models of fields 200 m (in red), 600 m (in green) and 1,800 m (in blue) above the top of magnetisation.

Table 9.5. Model statistics derived from inversion of the high-inclination magnetisation I_M = −75°.

Elevation (metres)	Body	Declination (degrees)	Inclination (degrees)	Error (degrees)	Centre offset (metres)	Centre azimuth (degrees)
1,800	A	315.0	−75.0	0.0	0	225
1,800	B	322.1	−72.2	3.4	119	178
1,800	C	329.2	−72.6	4.6	135	216
1,800	D	330.7	−77.4	4.4	130	268
1,800	E	315.0	−72.4	2.6	115	135
1,800	F	300.8	−72.5	4.7	136	55
600	A	315.3	−75.0	0.1	1	211
600	B	331.9	−65.8	10.7	211	179
600	C	343.6	−63.2	15.3	257	215
600	D	21.4	−77.5	15.1	234	269
600	E	315.0	−66.5	8.5	229	135
600	F	286.8	−62.9	15.4	257	56
200	A	316.2	−75.0	0.3	1	221
200	B	338.6	−58.5	18.7	284	179
200	C	343.0	−49.5	28.0	370	215
200	D	53.6	−69.4	27.1	306	269
200	E	316.5	−60.1	14.9	351	135
200	F	287.8	−49.0	28.4	369	55

Table 9.6. Model statistics derived from inversion of the low-inclination magnetisation I_M = −15°.

Elevation (metres)	Body	Declination (degrees)	Inclination (degrees)	Error (degrees)	Centre offset (metres)	Centre azimuth (degrees)
1,800	A	45.0	−15.0	0.0	0	0
1,800	B	45.3	−14.4	0.7	82	186
1,800	C	45.0	−14.7	0.3	88	225
1,800	D	44.7	−14.4	0.7	82	264
1,800	E	44.8	−14.3	0.8	83	140
1,800	F	45.0	−16.8	1.8	111	45
600	A	45.0	−15.0	0.0	0	0
600	B	46.0	−12.7	2.5	160	185
600	C	45.0	−13.4	1.6	189	225
600	D	44.0	−12.8	2.4	160	265
600	E	44.1	−12.3	2.8	185	140
600	F	45.0	−24.1	9.1	246	45
200	A	45.0	−15.0	0.0	0	0
200	B	47.1	−10.2	5.2	239	184
200	C	45.0	−9.6	5.4	316	225
200	D	42.9	−10.3	5.2	239	266
200	E	43.5	−9.7	5.5	304	138
200	F	45.0	−48.8	33.8	443	45

input model and their magnetisation directions converge towards its magnetisation direction. If the anomaly could be detected and successfully inverted at great distance (in a truly distal field) the inversion dipole model should be a spherical equivalent of the ellipsoid model with identical centre coordinates and magnetic moment (including magnetisation direction) as represented by the mesh view sphere in Fig. 9.8B.

The key model statistics for inversion of the high-inclination and low-inclination magnetisations are listed in Tables 9.5 and 9.6 respectively. These results are similar to the dipole-based $B_{z,z}$ analysis results in Tables 9.2 and 9.3. The inversion summary statistics presented in Table 9.4 are also close to the equivalent $B_{z,z}$ analysis statistics, confirming that the dipole-based $B_{z,z}$ analysis performs as expected for fields of dipole sources.

The statistics for estimation of the centre of magnetisation listed in Tables 9.2, 9.3, 9.5 and 9.6 are plotted in map form in Fig. 9.9. The key features recognisable in this figure are that:

1) the $B_{z,z}$ analysis (Fig. 9.9A) and dipole $B_{z,z}$ inversions (Fig. 9.9B) perform almost identically in estimating the centres of magnetisation
2) the plunge azimuth of each body causes a systematic displacement of its estimated centre. There are only minor differences between the displacements for the two magnetisation directions despite their wide angular separation
3) the absolute displacements of the estimated centres of magnetisation are a minimum for $B_{z,z}$ analyses and inversions at the highest elevation (plotted as symbols in blue in Figs 9.9 to 9.11). This is because the more distal field is least influenced by body shape, including plunge. $B_{z,z}$ analyses and inversions of the field at the shallowest elevation (plotted as symbols in red in Figs 9.9 to 9.11) are most strongly displaced towards the shallow up-dip extents of the plunging input models
4) the minimum displacements of the estimated centre of magnetisation from both the $B_{z,z}$ analyses and inversions are for the body that has a vertical axis with no plunge (body 'A').

Figure 9.10 plots the magnetisation direction estimates resulting from the $B_{z,z}$ analyses (Fig. 9.10A) and inversions (Fig. 9.10B). The symbols are identical to those used in Fig. 9.9. Figure 9.10 shows different dispersions of estimated magnetisation directions for the low-inclination magnetisation (plotted as points) and the steep-inclination magnetisation (plotted as crosses). For the low-inclination magnetisation almost all the error in magnetisation direction is in estimation of inclination. For the steeper-inclination magnetisation there is a more equal spread of directions in both declination and inclination. This difference exceeds the reduced significance of declination at high inclinations. The larger rotations of magnetisation direction away from the input

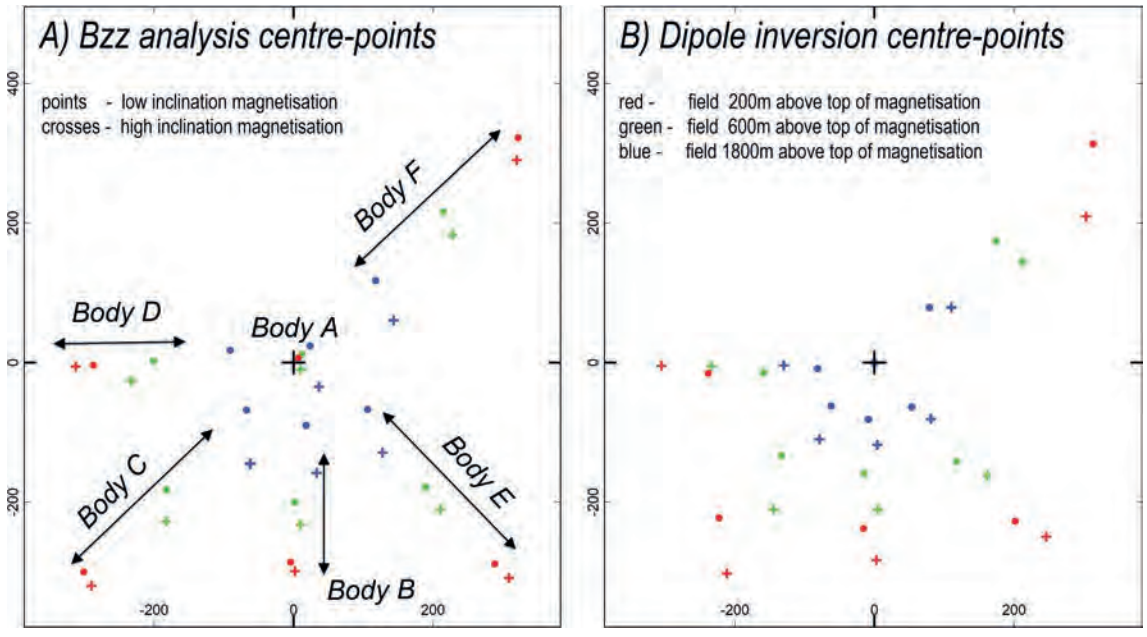

Fig. 9.9. Displacements of estimated centres of magnetisation: A) from the Bz,z analysis and B) from the dipole inversions.

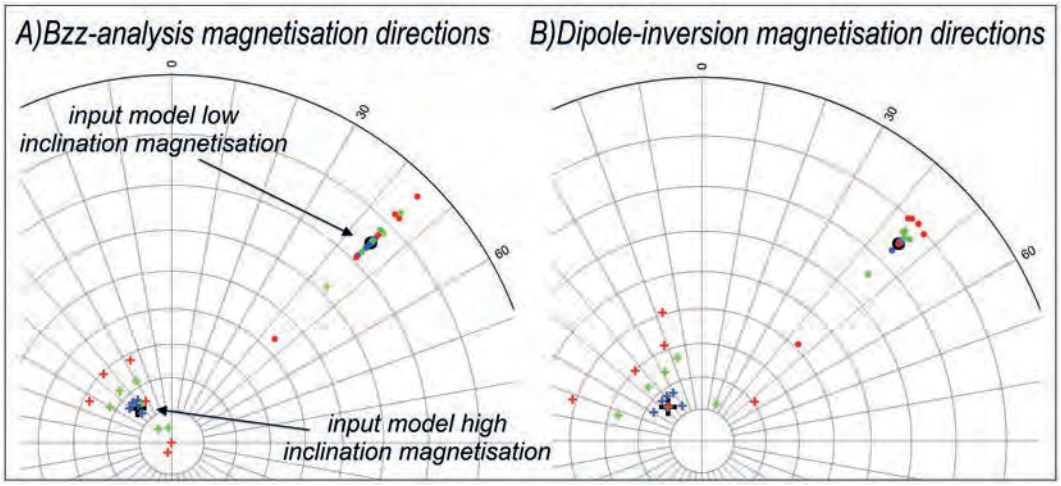

Fig. 9.10. $B_{z,z}$ analysis (A) and inversion model (B) magnetisation directions. Symbols are the same as in Fig. 9.9.

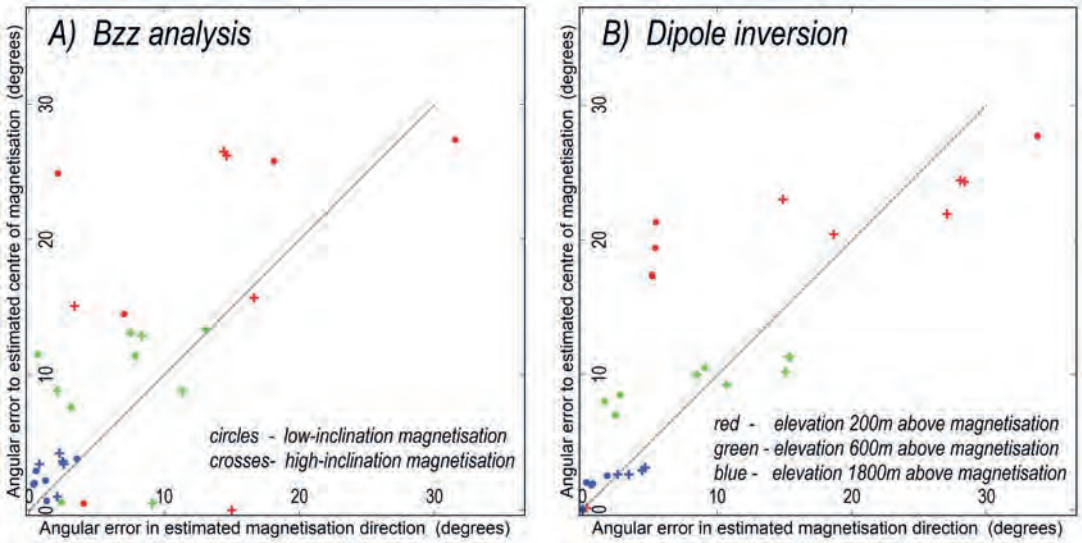

Fig. 9.11. Cross-plots of vertical axis: angular error to the centre of magnetisation (from the computation elevation) against horizontal axis: error in magnetisation directions. Symbols are the same as in Figs 9.9 and 9.10.

magnetisation direction are for $B_{z,z}$ analyses and inversions at the lowest elevation (the red symbols) consistent with those results also having the most substantial displacements of the estimated centres of magnetisation. This correspondence between displacement of estimated centre of magnetisation and error in estimated direction of magnetisation is highlighted in Fig. 9.11 which shows the angular error in positioning the centre of magnetisation (at the elevation of the computed magnetic field) cross-plotted against the angular error in estimated magnetisation direction. This figure emphasises the significant difference between strong influence of source plunge on the magnetic field proximal to the shallowest magnetisation (recorded with red symbols) and the much weaker influence on the more distal field (recorded with blue symbols).

9.4 A FIELD TEST OF THE ANALYSIS APPLIED TO REGIONAL TMI DATA FROM THE WHITE MOUNTAINS NATIONAL PARK AREA, EASTERN QUEENSLAND

Figure 9.12 shows the location of the test area in the White Mountains National Park of north-east Queensland. The area is covered by the Drummond and Galilee aeromagnetic survey (Geoscience Australia survey

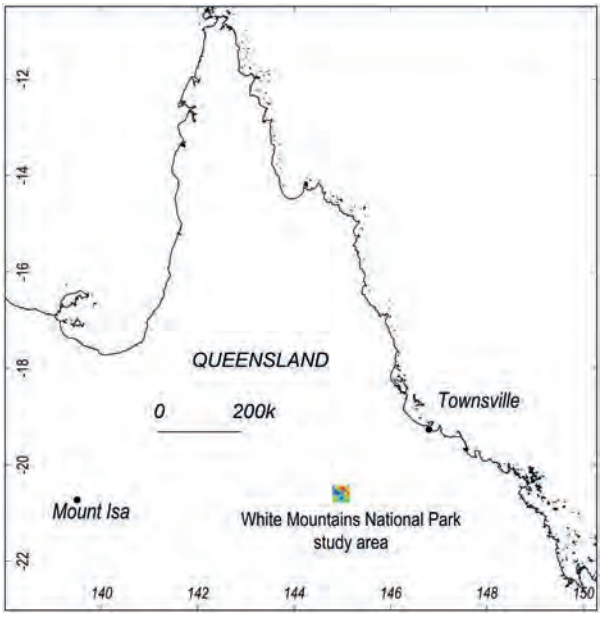

Fig. 9.12. Location of the study area in the White Mountains National Park, eastern Queensland.

number P793) flown on flightlines with azimuths of 070°–250° at a nominal ground clearance of 80 m and line spacing of 400 m. The data are available for download from the Geoscience Australia Geophysical Archive Data Delivery (GADDS). Figure 9.13A shows TMI variation across a part of that survey area. Broad, medium amplitude magnetic field variations are punctured by sharp, sub-circular anomalies of quite variable pattern, revealing that they are caused by shallow magnetisations of different orientation. Most of the anomalies are defined by measurements on a minimum of three lines, with some anomalies defined by measurements on up to five lines. The area lies within the Hughenden 1:250,000 geological map (Vine and Paine 1974). This is an area of limited outcrop but the most feasible source of the magnetisations are Cenozoic volcanics. Figure 9.13B shows the $B_{z,z}$ transform of the TMI grid that highlights the local anomalies of interest which are of dual polarities and have a wide range of patterns, indicating a wide range of magnetisation directions.

We individually inverted the 11 anomalies highlighted in Fig. 9.14 using clips of the flightline data as shown in the figure. For each anomaly a dedicated background field was defined using a second order polynomial surface. The model-computed field added to this regional was matched by inversion to the tie-line levelled data channel. The inversions used faceted body approximations to plunging pipes of elliptic cross-section with horizontal top and bottom faces. For each single body inversion there are 13 model free parameters: reference point easting, northing and elevation, two cross-section radii, long-axis azimuth, plunge, plunge azimuth, resultant magnetisation intensity, declination and inclination and background field slope and two planar gradients. Several of the anomalies that are immediately

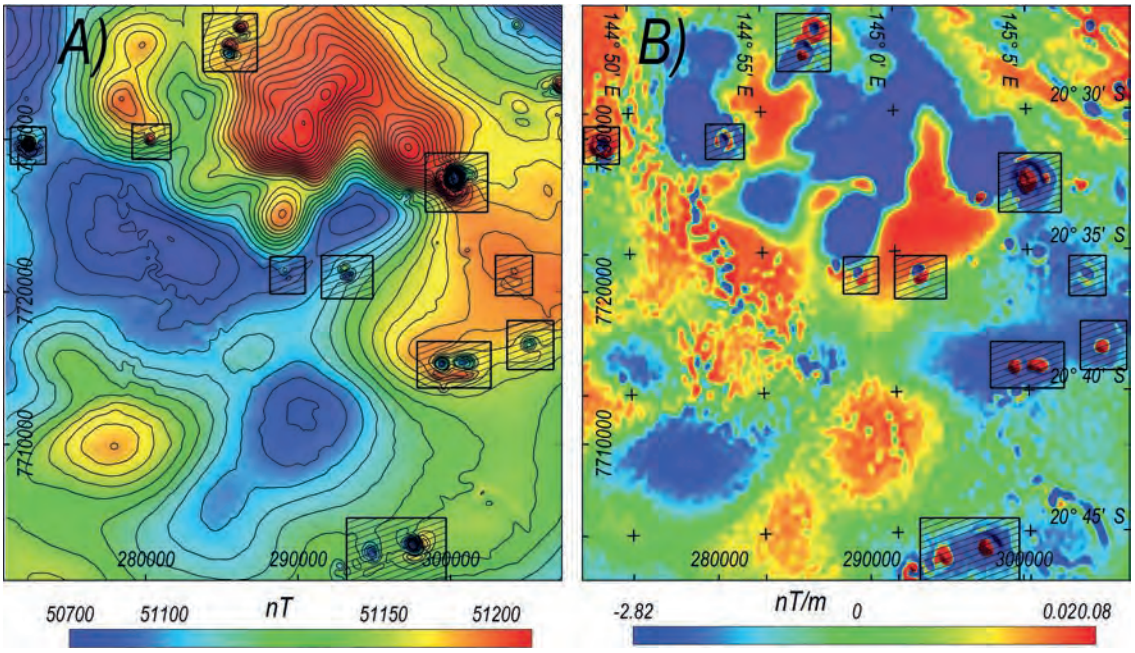

Fig. 9.13. A) TMI and B) the $B_{z,z}$ transform of TMI in the test area.

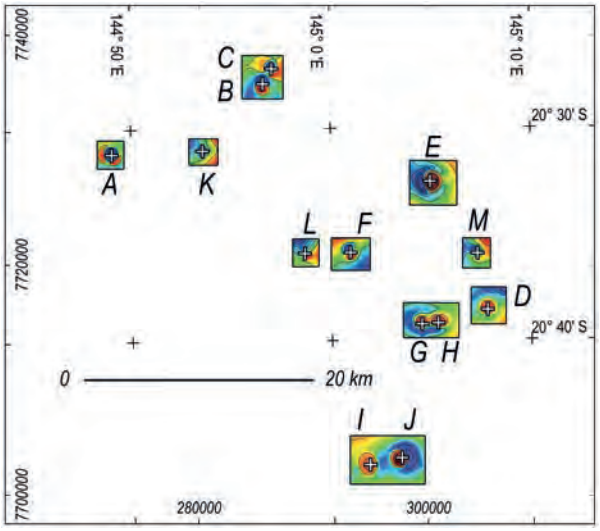

Fig. 9.14. Selected anomalies $B_{z,z}$.

adjacent to each other were investigated in combined double-body inversions because their magnetic fields overlap to the extent that it is difficult to analyse them separately. The magnetisation directions recovered from the inversions were checked by repeating the inversions with substituted triaxial ellipsoid bodies using the same data selections and initial background field definitions but completely independent forward modelling algorithms. In all cases the magnetisation directions from these check inversions were within 4 degrees of the directions for the pipe models. We report the pipe model results in Table 9.7 because these models provide estimates of depth to the top of magnetisation (a statistic that has little meaning or reliability for the ellipsoid models). Table 9.7 lists depth below sensor to the top of magnetisation and the major diameter for each model. The high ratio of the width of magnetisation to its depth below sensor reveal that the magnetic field has been measured in moderate proximity to the magnetisations.

Figure 9.15 shows a contour plot of the measured TMI field and of TMI forward computed from the post-inversion two-body inversion model for anomalies B and C. The goodness of fit is very high but the input data defining the anomaly is sparse. The peak and trough of each anomaly are defined on only single flightlines, with the adjacent lines serving mostly to constrain the extents of the anomalies. It is most likely that the peak and trough values of these anomalies, and the azimuths between those points would be different if the survey had been flown on lines with an offset of half the flightline spacing, or with infill lines flown between the existing lines. The $B_{z,z}$ analysis results are dependent on only those key statistics of peak and trough values and their locations but hopefully this sampling influence is diluted in inversion results derived for the complete population of anomalies.

Table 9.7. Pipe model spatial and magnetisation parameters.

Anomaly	Intensity of magnetisation (A/m)	Depth below sensor (metres)	Major X-section diameter (metres)	Magnetic moment ($A.m^2.10^6$)	Plunge angle (degrees)	Plunge azimuth (degrees)
A	2.624	87	422	118	65	7
B	1.458	44	546	80	63	178
C	1.326	85	312	182	69	175
D	2.357	410	478	49	45	0
E	1.550	64	1,188	725	50	176
F	4.881	243	370	19	44	0
G	0.845	180	564	93	89	180
H	1.120	262	1,068	144	73	180
I	1.410	487	942	120	60	142
J	2.985	514	682	274	84	177
K	2.205	225	130	10	85	148
L	1.017	107	236	7	50	3
M	.825	226	806	6	26	192

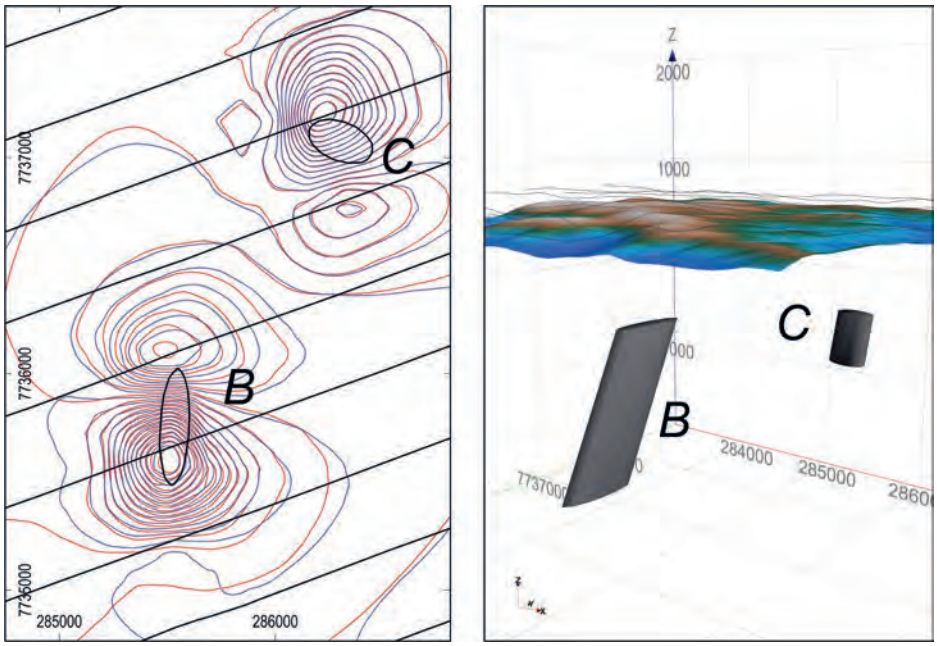

Fig. 9.15. A) measured (blue) and model-computed (red) TMI contours at 10 nT intervals for anomalies B and C with outlines of the source models, and B) perspective view of the models with flightlines and the ground surface.

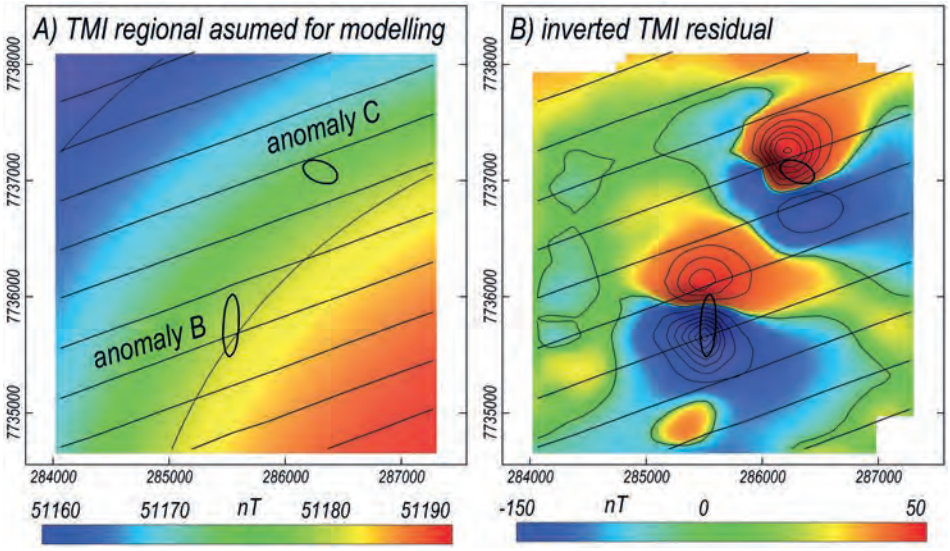

Fig. 9.16. A) regional and B) residual separations of the B and C anomalies (contour intervals 20 nT).

Figure 9.16A images the regional field variation assumed in inversion of anomalies B and C, and Fig. 9.16B images the residual field separation from that regional field. The two fields are contoured at the same interval, showing the regional field variations are subdued in comparison with the amplitudes of the residual anomalies. Superimposed regional fields change the asymmetry of the anomalies, and if this influence is not suppressed it leads to miscalculation of magnetisation direction. The major concern with the regional field is that its influence is amplified if upward continuation is applied to supress shape effects of the magnetisations. Figure 9.17A shows contours of $B_{z,z}$ derived from the TMI field of Fig. 9.15A after it had been upward continued by 400 m (in blue) and the corresponding contours of $B_{z,z}$ (in red) derived after 400 m upward continuation of the residual field separation shown in Fig. 9.16B. These contours are very similar and suggest that for these two

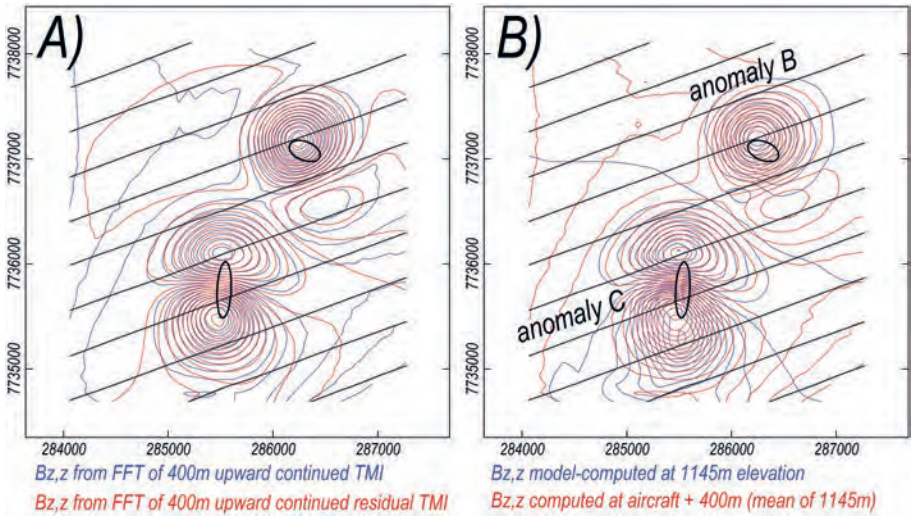

Fig. 9.17. $B_{z,z}$ at elevation 400 m above the survey elevation: A) from FFT upward continuation of measured and residual TMI, and B) model-computed at constant elevation and on survey lines +400 m.

anomalies, regional field separation before upward continuation is not critical (however we anticipate that this may not be the case for other anomalies). Upward continuation should ideally be applied to samples of the field equidistant from the magnetisation but this is not true of the field measurements. Of greater concern are sharp variations in elevation, particularly in areas of rugged relief where the sensor height above the magnetisation is variable both along flightlines and between them. Figure 9.17B shows contours of $B_{z,z}$ derived from the 400 m FFT upward continued residual TMI (in red) and (in blue) of $B_{z,z}$ directly computed from the pipe model after addition of 400 m to the flightline sensor elevation. Differences between these two estimates of $B_{z,z}$ vary with position (controlled by the terrain and its influence on flying height). They are highly disruptive in estimation of the detail of depth to the top of a magnetisation (see for instance Chapter 8) but fortunately have less effect on the more robust estimation of magnetisation direction. For all but the smallest and weakest of the anomalies, upward continuation is beneficial in estimation of magnetisation direction by the $B_{z,z}$ method proposed here. Over a particular area there is likely to be an optimal height for the population of anomalies that compromises attenuation of magnetisation shape effects and introduction of distortion from the upward continuation. Discovery of that 'best' upward continuation height will require testing with inversions of selected anomalies and accumulation of experience.

Table 9.8 lists differences between magnetisation directions recovered from $B_{z,z}$ analysis and dedicated TMI inversions. The mean difference is 10° and the maximum difference is 25°. Individual attention in developing the inversion solutions should result in higher reliability of those directions and we assume that differences between the inversion and $B_{z,z}$ analysis directions are predominantly due to higher error of the $B_{z,z}$ analysis. Inversions of even the most prominent anomalies are expected to have directional uncertainties of at least 5–10° (see Chapter 10) so the mean $B_{z,z}$ analysis error for this population of solutions may be of the order of 15° or more.

The magnetisation direction estimates are plotted in stereographic projection in Fig. 9.18. Dispersion of the individual anomaly inversion and $B_{z,z}$ analysis directions is much greater than expected for the apparent uncertainty in the estimates and is consistent with the wide range of anomaly patterns. The Cenozoic volcanics in this area are related to hot spot activity and may be extruded over a long period. The individual small and shallow bodies also cool quickly and may not faithfully record a stable geomagnetic field direction. Combination of these two factors may explain the wide scatter of magnetisation directions. Independent confirmation of magnetisation direction requires magnetic susceptibility and remanent magnetisation measurement on oriented samples that in this area of sparse (and probably weathered) outcrop would mostly require availability of drillhole cores. Alternatively, the individual anomalies could be measured at lower elevation and higher spatial resolution using drones or ground magnetic surveys to support more diagnostic inversion and $B_{z,z}$ analysis.

Table 9.8. Comparison of $B_{z,z}$ analysis and pipe model inversion magnetisation directions.

Anomaly	Peak-trough amplitude ratio	$B_{z,z}$ analysis declination (degrees)	$B_{z,z}$ analysis inclination (degrees)	Inversion declination (degrees)	Inversion inclination (degrees)	Angular difference (degrees)
A	14.2	334	−78	1	−80	5
B	1.7	3	16	7	16	4
C	4.7	334	−45	11	−46	25
D	13.6	206	77	192	76	3
E	4.0	259	41	255	48	8
F	1.0	340	1	335	−8	10
G	6.6	213	55	188	54	14
H	5.0	215	48	189	47	18
I	8.8	84	64	95	64	5
J	5.1	74	48	67	50	5
K	8.7	61	−64	36	−62	11
L	1.2	329	−5	334	8	14
M	3.3	350	−35	346	−42	8

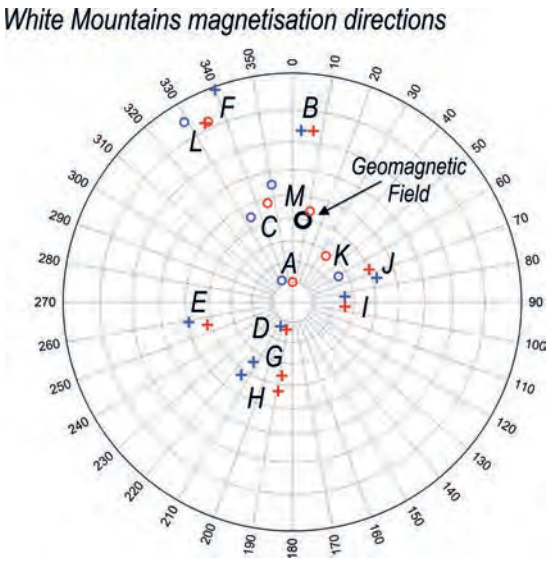

Fig. 9.18. White Mountains magnetisation directions. Red – from $B_{z,z}$ analysis and Blue – from model inversions. Circles are negative inclination, cross are positive inclination.

9.5 CONCLUSIONS

We have established that over compact magnetisations, $B_{z,z}$ anomalies derived by FFT analysis of moderate- to high-resolution TMI data can provide approximate estimates of magnetisation direction. The declination of magnetisation is indicated by the azimuth of the $B_{z,z}$ anomaly and the inclination of magnetisation is indicated by its peak to trough amplitude ratio. The analysis is almost independent of the geomagnetic field direction. Magnetisation estimates derived from measurements close to a magnetisation are corrupted by the influence of the distribution of magnetisation. In more distal fields, magnetisation shape effects are less significant but reduced anomaly amplitudes cause problems in reliable anomaly separation from background and overlapping fields. We have demonstrated recovery of known magnetisation directions from $B_{z,z}$ analysis of synthetic data and shown that magnetisation directions consistent with parametric inversion results are recovered from $B_{z,z}$ analysis of magnetic field data measured above a series of small Cenozoic volcanic bodies in Queensland.

REFERENCES

Baranov V, Naudy H (1964) Numerical calculation of the formula of reduction to the magnetic pole. *Geophysics* **29**, 67–79. doi:10.1190/1.1439334

Beiki M, Clark DA, Austin JR, Foss CA (2012) Estimating source location using normalised magnetic source strength estimated from gradient tensor data. *Geophysics* **77**, J23–J37. doi:10.1190/geo2011-0437.1

Blakely RJ (1995) Potential theory in gravity and magnetic applications. Cambridge University Press.

Blakely RJ, Simpson RW (1986) Approximating edges of source bodies from magnetic or gravity anomalies. *Geophysics* **51**, 1494–1498. doi:10.1190/1.1442197

Caratori Tontini F, Pedersen LB (2008) Interpreting magnetic data by integral moments. *Geophysical Journal International* **174**, 815–824. doi:10.1111/j.1365-246X.2008.03872.x

Clark DA (2012) New methods for interpretation of magnetic vector and gradient tensor data I: eigenvector analysis and the normalised source strength. *Exploration Geophysics* **43**, 267–282. doi:10.1071/EG12020

Clark DA (2013a) New approaches to dealing with remanence: magnetic moment analysis using tensor invariants and remote determination of *in-situ* magnetisation using a static tensor gradiometer. ASEG-PESA Conference, Melbourne, Extended Abstract 1–7.

Clark DA (2013b) New methods for interpretation of magnetic vector and gradient tensor data II: application to the Mount Leyshon anomaly, Queensland, Australia. *Exploration Geophysics* **44**, 114–127. doi:10.1071/EG12066

Clark DA (2014) Methods for determining remanent and total magnetisations of magnetic sources – a review. *Exploration Geophysics* **45**, 271–304. doi:10.1071/EG14013

Cooper G, Cowan D (2003) The application of fractional calculus to potential field data. *Exploration Geophysics* **34**, 51–56. doi:10.1071/EG03051

Foss CA, Austin JR (2023) Distal, proximal and sweet spot limitations in source information content of magnetic field data. 4th AEGC Conference, 13–18 March 2023, Brisbane, Australia, 6p.

Foss CA, McKenzie B (2011) Inversion of anomalies due to remanent magnetisation: an example from the Black Hill Norite of South Australia. *Australian Journal of Earth Sciences* **58**, 391–405. doi:10.1080/08120099.2011.581310

Helbig K (1963) Some integrals of magnetic anomalies and their relation to the parameters of the disturbing body. *Zeitschrift für Geophysik* **29**, 83–96.

Lourenço JS, Morrison HF (1973) Vector magnetic anomalies derived from measurements of a single component of the field. *Geophysics* **38**, 359–368. doi:10.1190/1.1440346

McKenzie KB (2020) The magnetic gradient tensor of a triaxial ellipsoid, its derivation and its application to the determination of magnetisation direction. *Exploration Geophysics* **51**, 609–641. doi:10.1080/08123985.2020.1726176

McKenzie KB (2022) The magnetic field and magnetic gradient tensor for a right circular cylinder. *Exploration Geophysics* **53**, 329–358. doi:10.1080/08123985.2021.1951117

Medeiros WE, Silva JBC (1995) Simultaneous estimation of total magnetisation direction and 3-D spatial orientation. *Geophysics* **60**, 1365–1377. doi:10.1190/1.1443872

Phillips JD, Hansen RO, Blakely RJ (2007) The use of curvature in potential field interpretation. *Exploration Geophysics* **38**, 111–119. doi:10.1071/EG07014

Pratt DA, McKenzie KB, White AS (2014) Remote remanence estimation (RRE). *Exploration Geophysics* **45**, 314–323. doi:10.1071/EG14031

Schmidt PW, Clark DA (1998) Calculation of magnetic components and moments from TMI: a case study from the Tuckers igneous complex, Queensland. *Exploration Geophysics* **29**, 609–614. doi:10.1071/EG998609

Schmidt PW, Clark DA (2006) The magnetic gradient tensor: its properties and uses in source characterization. *The Leading Edge* **25**, 75–78. doi:10.1190/1.2164759

Vine RR, Paine AGL (1974) Hughenden, Queensland – 1:250 000 Geological Series. Bureau of Mineral Resources of Australia. Explanatory Notes SF/55–1

Zietz I, Andreasen GE (1967) Remanent magnetisation and aeromagnetic interpretation. *Mining Geophysics* **2**, 569–590.